Journal of Fluorine Chemistry 208 (2018) 36–47

Contents lists available at ScienceDirect

Journal of Fluorine Chemistry

journal homepage: www.elsevier.com/locate/fluor

A new perfluoromethyl aminoenone derivative and the role of the hydrogen bonding in the intra- and intermolecular interactions

Mariana Rocha[a], Diego M. Gil[a,*], Gustavo A. Echeverría[b], Oscar E. Piro[b], Jorge L. Jios[c], Sonia E. Ulic[d,e,**]

[a] INQUINOA (CONICET-UNT), Instituto de Química Física, Facultad de Bioquímica, Química y Farmacia, Universidad Nacional de Tucumán, San Lorenzo 456, T4000CAN San Miguel de Tucumán, Tucumán, Argentina
[b] Departamento de Física, Facultad de Ciencias Exactas, Universidad Nacional de La Plata e IFLP (CONICET, CCT-La Plata), C.C. 67, 1900 La Plata, Argentina
[c] UNIDAD PLAPIMU-LASEISIC (UNLP-CIC), Departamento de Química, Facultad de Ciencias Exactas, Universidad Nacional de La Plata, 47 esq. 115, 1900 La Plata, Argentina
[d] CEQUINOR (CONICET-UNLP), Facultad de Ciencias Exactas, Universidad Nacional de La Plata, Bv. 120 N° 1465, 1900 La Plata, Argentina
[e] Departamento de Ciencias Básicas, Universidad Nacional de Lujan, Rutas 5 y 7, 6700 Lujan, Buenos Aires, Argentina

ARTICLE INFO

Keywords:
β-Aminoenone tautomer
Crystal structure
DFT calculations
Hydrogen bonding
Hirshfeld surface analysis

ABSTRACT

The structure of a new perfluoromethyl derivative, *(Z)*-4,4,4-trifluoro-1-(2-hydroxyphenyl)-3-(methylamino)-2-buten-1-one **(1)**, was investigated in both crystalline state and solution since the prototropy enable the existence of three tautomeric species in equilibrium. The preference in the configurational E/Z arrangement is strongly dependent on the intramolecular hydrogen bond interactions. The vibrational and electronic spectra of **1** were discussed and assigned by using DFT calculations. The crystal, solved by single-crystal X-ray diffraction, shows the prevalence of the tautomer aminoenone over the imino-enol and imino-ketone forms. Therefore, an almost planar molecular conformation is observed due to the formation of two intramolecular amino and phenolic hydrogen bonds to the same carbonyl oxygen acceptor atom that stabilize the *Z* configuration. The molecular packing is held by the O—H···O(keto) and N—H···O hydrogen bonds, F···F, C—H···π and π-stacking interactions that contribute to the crystal stabilization. The intra and intermolecular contacts were also characterized by Natural Bond Orbital (NBO) analysis and Atoms in Molecules (AIM) approach. Hirshfeld surfaces and their associated fingerprint plots were generated for **1** and for a related structure, to visualize different intermolecular interactions and their relative contributions to the total surface.

1. Introduction

The β-aminoenone derivatives, i.e. molecules containing the conjugated O=C–C=C–N moiety, are important organic compounds that have been used as intermediates or building blocks in synthetic [1] and medicinal chemistry [2–4], but they also have biological activities. Recent studies indicate that aminoenones have analgesic, papaverine-like, hypoglycaemic, and anti-convulsant activities [5–8]. The anticonvulsant effects of some aminoenoles have been attributed to suppression of tetrodotoxin (TTX)-sensitive sodium channels, enhancement of extracellular γ-aminobutyric acid levels, activation of α 2-adrenoceptors and reversible suppression of glutamate-mediated excitatory postsynaptic currents [6–8]. These compounds are very important precursors for the synthesis of coordination compounds since they can coordinate as monodentate, bidentate or tridentate structures with metal ions. In the last decade, some metal complexes with aminoenones have been reported, including zirconium and titanium complexes with derivatives of N-(2-hydroxyalkyl) imines [9,10] and Ni(II), Cu(II) and Pd(II) complexes with tri and tetradentate aminoenones [11].

β-Aminoenone compounds are present in a tautomeric equilibrium between the iminoenol, iminoketo and aminoenone forms (see Scheme 1), as was reported by Hidalgo et al. [12]. A similar tautomerism is observed in different Schiff bases containing aromatic *o*-hydroxyaldehydes [13–15]. A reversible intramolecular proton transfer, driven by electrostatic differences, is observed between the oxygen and nitrogen atoms of the salicylideneimine fragment [13–15], which promotes the delocalization of the aromatic π-electron system leading to a quinoid form, also related with its canonical zwitterionic form. Different spectroscopies (UV–vis, infrared, Raman, ^{1}H and ^{13}C NMR) and mass spectrometry have been used to study the tautomeric equilibrium

* Corresponding author.
** Corresponding author at: CEQUINOR (CONICET-UNLP), Facultad de Ciencias Exactas, Universidad Nacional de La Plata, Bv. 120 N° 1465, 1900 La Plata, Argentina.
E-mail addresses: dmgil@fbqf.unt.edu.ar (D.M. Gil), sonia@quimica.unlp.edu.ar (S.E. Ulic).

https://doi.org/10.1016/j.jfluchem.2018.01.001
Received 29 November 2017; Received in revised form 29 December 2017; Accepted 2 January 2018
Available online 31 January 2018
0022-1139/

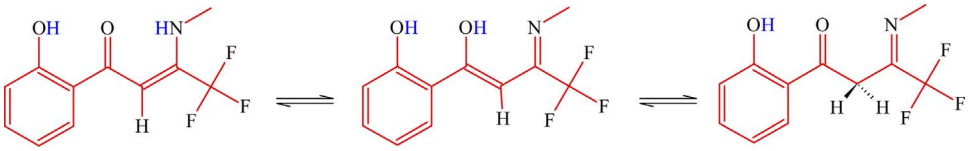

Aminoenone form (**I**) Iminoenol form (**II**) Iminoketone form (**III**)

Scheme 1. Possible tautomeric forms in equilibrium for the title compound.

of the three possible forms of the aminoenones [12,16]. The crystal structure of different β-aminoenone derivatives have been solved by single crystal X-ray diffraction methods [17–20]. For all these structures, the O═C−C═C−N fragment is planar favoring the N−H···O═C hydrogen bonds.

β-Aminoenone derivatives were usually synthesized by condensation of β-diketones with primary amines. Organic fluorine-containing compounds have attracted great interest in the fields of life and materials sciences. The substitution of hydrogen atoms by fluorine usually alters the physical and chemical properties of the compounds due to the influence of the fluorine atom on their electronic properties and stability resulting in greater resistance to metabolic degradation [21].

In this work, the synthesis and characterization of 4,4,4-trifluoro-1-(2-hydroxyphenyl)-3-(methylamino)-2-buten-1-one **(1)** is reported. The compound was characterized by IR, Raman, UV–vis and ^{1}H and ^{13}C NMR spectroscopy. The structure has been solved by single crystal X-ray diffraction methods and the crystal packing was evaluated by using the Hirshfeld surface analysis. It has allowed visualizing the proportion and nature of the intermolecular interactions present in the structure that are not readily apparent by examining only the crystal structure. The structural analysis was performed in comparison with a closely related structure previously reported in our group [12]. The vibrational and electronic properties were studied in conjunction with quantum chemical calculations using DFT methods. The Natural Bond Orbital (NBO) analysis was performed and the donor-acceptor energies were calculated by using the second-order perturbation theory. Besides, atoms in molecules (AIM) topological analysis of the electron charge density was carried out to characterize intra and intermolecular hydrogen bonds observed in the single crystal.

2. Experimental

2.1. Synthesis

The title compound was prepared as follows: In a round-bottom flask a mixture of 2-trifluoromethylchromone (2 mmol, 0.380 g) and methylamine (0.5 mmol, 0.0155 g) in ethanol were continuously stirred at room temperature for 30 min. After isolation, the yellow crystalline solid was re-crystallized from hot ethanol. Suitable crystals for X-ray diffraction measurements were obtained from slow evaporation of an ethanolic solution.

2.1.1. (Z)-4,4,4-Trifluoro-1-(2-hydroxyphenyl)-3-(methylamino)-2-buten-1-one (1)

Yellow crystalline solid; Yield: 80%; melting point: 112 °C; ^{1}H NMR ($CDCl_3$, δ ppm, J Hz): 12.71 (s, OH), 10.34 (br.s, NH), 7.66 (d, H2, J = 8), 7.40 (t, H4, J = 7.7), 6.95 (d, H3, J = 8), 6.86 (t, H5, J = 7.7), 6.23 (s, H8), 3.15 (d, J = 5, CH_3); ^{13}C NMR ($CDCl_3$, δ ppm, J Hz): 193.9 (C═O), 162.3 (C6), 151.4 (q, C9, 2JCF = 30), 135.0 (C4), 128.1 (C2), 120.1 (s, C1), 119.9 (q, C10, 1JCF = 278), 118.8 (C3), 118.5 (C5), 88.1 (q, C8, 3JCF = 5), 31.0 (q, C11, 4JCF = 3.5); ^{19}F NMR ($CDCl_3$, δ ppm): 69.0 (s).

2.2. Instrumentation

The melting point of the crystals was determined using Differential Scanning Calorimetry (DSC) measurements on a Perking Elmer Pyris DSC 6 calorimeter. The ^{1}H (600.1 MHz), ^{13}C (150.9 MHz) and ^{19}F (564.7 MHz) NMR spectra were recorded on a Bruker Advance III spectrometer in $CDCl_3$ using tetramethylsilane (TMS) as internal reference (See Figs. S2–S3). The solid state IR absorption spectra (in KBr pellets) were measured on a FTIR Perkin Elmer GX1 in the 4000–400 cm^{-1} range with 2 cm^{-1} of spectral resolution. The Raman dispersion spectra of the solid was measured at room temperature in the range 3500–50 cm^{-1} on a Thermoscientific DXR Raman microscope using a diode-pump, solid state green laser of 532 nm. The spectral resolution was 5 cm^{-1} and 10 expositions of 2 s were accumulated for the sample, to achieve sufficient signal to noise ratio. UV–vis spectra were recorded in ethanol using a quartz cell (10 mm optical path length) on a ChromTech CT-5700 UV/vis spectrophotometer at 2.0 nm spectral bandwidth. Measurements were carried out in the spectral region from 190 to 1100 nm.

2.3. X-ray diffraction data and structural refinement of (1)

The measurements were performed on an Oxford Xcalibur, Eos, Gemini CCD diffractometer with graphite-monochromated MoKα (λ = 0.71073 Å) radiation. X-ray diffraction intensities were collected (ω scans with ϑ and κ-offsets), integrated and scaled with CrysAlisPro [22] suite of programs. The unit cell parameters were obtained by least-squares refinement (based on the angular settings for all collected reflections with intensities larger than seven times the standard deviation of measurement errors) using CrysAlisPro. Data were corrected empirically for absorption employing the multi-scan method implemented in CrysAlisPro. The structure was solved by intrinsic phasing with SHELXT of the SHELX suit of programs [23] and the non-H atoms refined by full-matrix least-squares procedure with SHELXL of the same package. All but the methyl H-atoms were located in a difference Fourier map and refined at their found positions with isotropic displacement parameters. The methyl H-atoms were refined as a rigid group allowed to rotate around the C−C bonds such as to maximize the sum of the observed residual electron density at their calculated positions. As a result the $-CH_3$ group converged to staggered angular conformation. Crystal data and refinement results are summarized in the Supplementary information (Table S1) and all the structural parameters are shown in the Supplementary information (Tables S3–S5). Crystallographic structural data have been deposited at the Cambridge Crystallographic Data Centre (CCDC). Any request to the Cambridge Crystallographic Data Centre for this material should quote the full literature citation and the reference numbers CCDC 1573238.

2.4. Computational details

Molecular quantum chemical calculations were performed with GAUSSIAN 03 program package [24], using the B3LYP [25,26] method and 6-311 + + G(d,p) basis sets. The calculated vibrational properties correspond, in all cases, to potential energy minima with no imaginary values for the frequencies. The Potential Energy Distribution (PED) has been calculated at B3LYP/6-311 + + G(d,p) level with the VEDA4 program [27,28]. Electronic transitions were calculated within the Time-Dependent Density Functional Theory (TD-DFT) [29] taking into account implicitly the solvent effect (ethanol) at the same level of theory used for optimization and frequency calculations (B3LYP/6-311 + + G(d,p)) by using the Polarizable Continuum Model (PCM) [30].

Natural population analysis and second-order donor → acceptor interaction energies were calculated at B3LYP/6-311 + + G(d,p) approximation using NBO analysis [31]. The nature of intra- and intermolecular hydrogen bonds was evaluated using the AIM approach by means of AIM2000 software [32]. In the topological analysis (AIM), the bond critical points (BCP) give detailed information on the relative strength of the hydrogen bond, obtained in term of electron density (ρ) and its Laplacian $\nabla^2(\rho)$. The energy of the intra- and intermolecular hydrogen bonds were estimated using the empirical formula proposed by Espinosa and co-workers [33], based on the electron density distribution at the (3, −1) BCPs of the hydrogen bonds.

2.5. Hirshfeld surface calculations

Hirshfeld surfaces and their associated 2D fingerprint plots [34–36] were generated by means of CrystalExplorer 3.1 software [37]. The normalized contact distance (d_{norm}) based on both d_e (the distance from the point to the nearest nucleus external to the surface) and d_i (the distance to the nearest nucleus internal to the surface) and vdW radii of the atom, enables the identification of regions with significative intermolecular interactions. A color scale of red (shorter than vdW separation) – white (equal to vdW separation) – blue (longer than vdW separation) has been used to evaluate the intermolecular interactions present in the crystal. The 3D-d_{norm} Hirshfeld surfaces were mapped over a fixed color scale of −0.25 a.u. (red) to 1.05 a.u. (blue), shape index mapped in the color range of −1.0 a.u. (concave) to 1.00 a.u. (convex) and curvedness in the range of −4.0 a.u. (flat) to 4.0 a.u. (singular). The 2D-fingerprint plots were displayed using the translated 0.6–2.6 Å range and including reciprocal contacts.

3. Results and discussion

3.1. Crystal structure and its comparison with the calculated molecular geometry

An ORTEP drawing of the X-ray diffraction crystal structure of compound **(1)** is shown in Fig. 1, together with a view of the molecular structure computed at the B3LYP/6-311 + + G(d,p) approximation. The experimental geometrical parameters are compared in Table S2 with the corresponding calculated ones at B3LYP/6-311 + + G(d,p) approximation.

The tautomeric form adopted for the title compound in the crystal is the aminoenone **I**. Clearly, both intramolecular amino and phenolic hydrogen atoms bonded to the same carbonyl oxygen acceptor atom play a decisive role not only in the adopted tautomeric form but also in the *E/Z* configuration. In the last isomerism, the *Z*- is stabilized over the *E*-configuration mainly by the above described strong intramolecular hydrogen bonds favored by the planar arrangement and the synergistic interplay between π-delocalization and hydrogen-bonds strengthening (RAHB model) [38]. Other β-aminoenones show the same *Z* configurational preference [12,38,39].

Table 1
Parameters of Intra and Intermolecular contacts for compound **1** (Å, °).

D−H···A	d(D−H)	d(H···A)	d(D···A)	< (D−H···A)
Intramolecular				
N−H···O2	0.96	1.88	2.6523(1)	136
O1−H···O2	0.90	1.72	2.5294(1)	147
C8−H···F3	0.91	2.29	2.6840(1)	106
C11−H11A···F1	0.96	2.50	2.8920(2)	105
C11−H11C···F2	0.96	2.53	3.0483(2)	114
Intermolecular				
N−H···O1^{i}	0.96	2.36	3.1131(2)	135
O1−H···O2^{i}	0.90	2.45	2.9760(2)	118
C11−H11B···O1^{ii}	0.96	2.72	3.359(2)	124
C4−H4···F3^{iii}	0.99	2.82	3.428(2)	121
C3−H3···F3^{iii}	0.94	2.81	3.400(1)	122

Symmetry codes: (i) −x,1-y,-z; (ii) −x + 1,-y + 2,-z + 1; (iii) −x + 1/2 + 1, +y + 1/2, −z + 1/2 + 1.

Bond lengths and angles are in general agreement with expectations from organic chemistry rules. In particular, the C−C bond lengths in the phenol ring are in the range from 1.368(4) to 1.397(3) Å, as expected for a resonant bond structure. For the enone group, the bond lengths of the carbonyl C7═O2 and the conjugated C8−C9 bond are 1.259(3) and 1.371(3) Å, respectively, indicating a typical double-bond character of these bonds. However, the C9-N bond length for the investigated compound is shorter (1.331(3) Å) than the average single C−N bond length of 1.458(3) Å. The optimized molecular structure shows the double bond character of these bonds as shown in Fig. 1 (right, dashed lines).

As shown in Fig. 1(a) and Table 1, the carbonyl O2 atom acts as acceptor forming bifurcated intramolecular hydrogen bonds with the N−H and the O1−H groups. These results are in accordance with the expected bond delocalization in the compound and confirmed by C11−N−C9 and C8−C9−N angles of 128.9(2)° and 124.7(2)°, which is consistent with the sp^2 hybrid character of N and C9 atoms. As shown in Fig. 1, the molecule maintains the *cis* configuration with respect to C8−C9 double bond.

Interestingly, non-classical C8−H···F3, C11−H11A···F1 and C11−H11C···F2 intramolecular hydrogen bonds are present in the crystalline state.

The phenol ring and the O═C−C−C═C−N moiety are nearly planar, as reflected by C6−C1−C7−C8, C1−C7−C8−C9 and C11−N−C9−C8 torsion angles near to ± 180°. As can be appreciated from Table S2, it is observed a very good agreement between calculated and experimental geometrical parameters.

An exhaustive analysis of the structural parameters of compound **1** (Table 1) indicates that the supra-molecular assembly is governed by

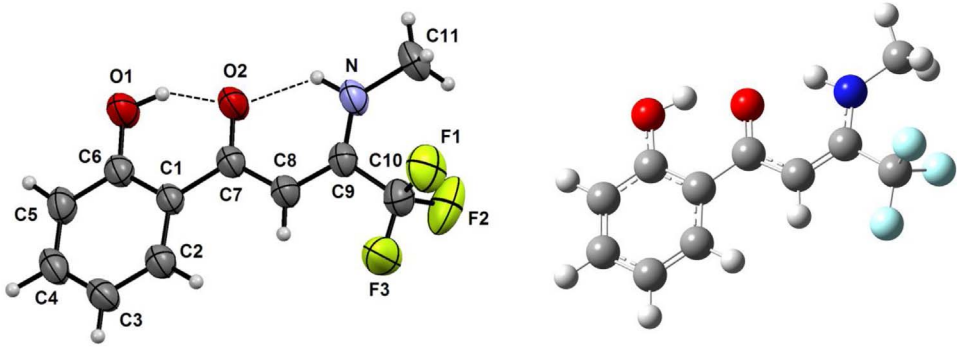

Fig. 1. (a) X-ray solid state molecular structure of compound **(1)** showing the labeling of the non-H atoms and their displacement ellipsoids at the 30% probability level (b) view of computed molecular structure at B3LYP/6-311 + + G(d,p) approximation.

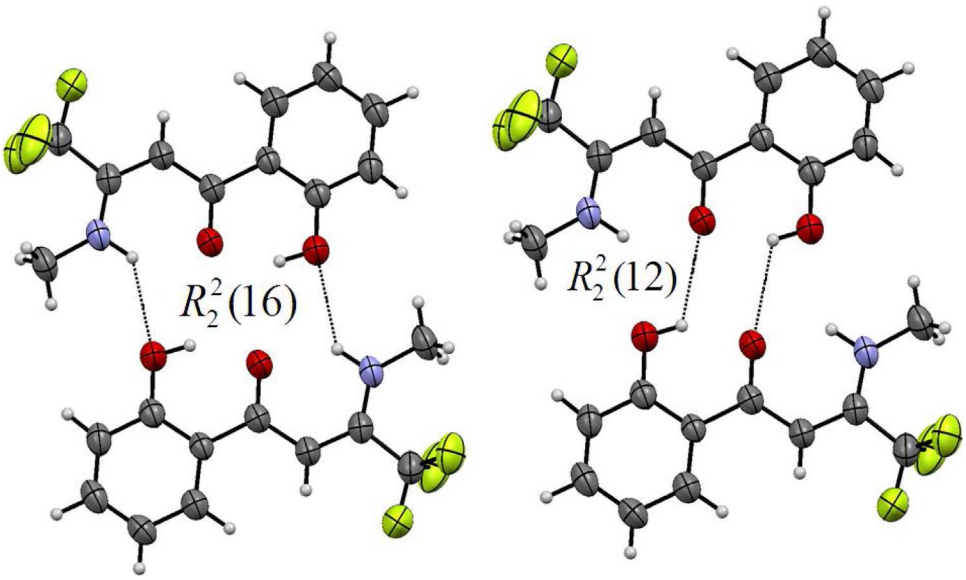

Fig. 2. Crystal packing of compound (1) showing centre-symmetric dimers. Inter-molecular hydrogen bonding interactions are shown by dashed lines.

N—H···O1 and O1—H···O2 hydrogen bonds. The N—H···O2 interaction associates neighboring molecules through phenol hydroxyl and the N—H fragments leading to centre-symmetric $R_2^2(16)$ dimers (See Fig. 2) with a N···O distance of 2.6523(1) Å.

In addition, other O···H contacts due to O1—H···O2 hydrogen bonds link the molecules into centre-symmetric dimers, giving $R_2^2(12)$ graph-set motifs (Fig. 2, Table 1). As mentioned, these forces could be considered as one of the main intermolecular interactions driven molecular packing. However, when molecules approach each other, the aminoenone impose severe restrictions on the geometry of the intermolecular O—H···O and N—H···O hydrogen bonds that can be formed, since the hydroxyl and amine groups are already involved in intramolecular hydrogen bonds. These limitations are visualized by the significantly deviation from the ideal geometry of the intermolecular O—H···O and N—H···O hydrogen bonds, characterized by small angle values at the hydroxyl or amine hydrogen atoms as well as the large H···O and H···N distances (see Table 3). Contrary, in (*Z*)-4,4,4-Trifluoro-3-(2-hydroxyethylamino)-1-(2-hydroxyphenyl)-2-buten-1-one [12] this restriction is partially released due to it has an additional $-(CH_2)_2OH$ group. This moiety is slightly departing from the molecular plane but folded back to allow intermolecular O—H···O hydrogen bonds closer to the ideal contact geometry (i.e. more linear and shorter H···O distance) involving the terminal hydroxyl of one molecule and the phenol oxygen of a 2-fold screw-axis symmetry-related neighboring molecule.

The supra-molecular assembly of compound **(1)** also suggests the existence of π···π and C—H···π interactions (Fig. 3). A Cg1···Cg1 interaction [inter-centroid distance of 4.9345(3) Å] presents an off-set arrangement involving two neighboring phenyl rings (Cg1 centroid) and represents a weak π-stacking interaction. The C—H···Cg1 contact [d (H···Cg1) = 3.580(1) Å] completes the supra-molecular network. This interaction involves the Cg1 centroid and one hydrogen of the methyl group attached to the N atom.

The centre-symmetric dimers build ribbons along the [110] crystallographic direction suggesting that C—H···F hydrogen bonds (See Fig. 4) might play some role in molecular packing, although the H···F distances too much longer than the sum of van der Waals radii of hydrogen and fluorine atoms indicate that they should be very weak or even not contribute at all to the crystal stabilization (see Table 1). A similar behavior has been observed in the crystal structure of the molecule *N*-[2-(trifluoromethyl)phenyl]benzamide, where the packing was stabilized by strong N—H···O=C, weak C—H···O=C and short C—H···F hydrogen bonds [40]. For this compound, the participation of the acidic hydrogen atoms (adjacent to the CF_3 group) in the hydrogen bonds was evidenced through the key symmetry elements of the corresponding spatial group, which crystallized in the rare tetragonal non-centre symmetric space group $P4_1$. In the last twenty years, the role of intermolecular interactions involving organic fluorine has been analyzed both experimentally and theoretically [41–43]. For example, in the crystal structure of some organic compounds such as fluorine substituted isoquinolines [44], trifluoroacetophenones [45] and pyridines [46], the importance of weak C—H···F hydrogen bonds was observed in the absence of any strong hydrogen bond donor. Choudhury et al. [47] reported the crystal structure of pentafluorophenylprop-2-ynylcarbonate, showing that its crystal packing was dominated by C—H···F interactions over C—H···O hydrogen bonds. This observation promoted the debate about the significance of C—H···F hydrogen bond.

Generally, halogen–halogen interactions are divided into two categories, namely type I and type II (See Fig. S4, Supplementary information) [48]. Both types appear frequently in the literature wherein heavier halogen tends to form type II more frequently while fluorine appears to form mainly type I intermolecular interactions. Type I contacts provide very weak stabilization to the crystal packing. It is essentially a van der Waals interactions arising when two halogen atoms minimize repulsion by interfacing the neutral regions of their electrostatic potential surfaces. In accordance to the very low polarizability of the fluorine atom, its participation in F–F interactions was questioned. In compound (**1**) trifluoromethyl groups, symmetry related by a two-fold screw axis, are linked by C10—F2···F3^{iv}—C10^{iv} (iv: 1/2-x, 1/2 + y, 3/2-z) interactions of type I as evidenced from the F2···F3 distance of 2.9646(1) Å and C10—F2···F3^{iv} and F2···F3^{iv}—C10^{iv} angles of 144.6(2) and 131.2(2)° respectively. This halogen···halogen contact develops an extended pattern along the crystallographic *b*-axis, connecting centre-symmetric dimers ribbons to each other (See Fig. 4).

3.2. Prevalence of the aminoenone tautomer in solution analyzed by NMR spectroscopy

In the ^{1}H, ^{13}C and ^{19}C NMR spectra (see Figs. S1–S3, Supplementary information), only one set of signals corresponding to a single tautomer is detected in solution, e.g. the ^{19}F NMR shows only one signal (sharp singlet at 69.0 ppm). Since different equilibria can be established in solution, the present tautomer corresponds to one of the three possible represented in Scheme 1. After inspection of the NMR spectra, the identity of this species could be unambiguously elucidated according to the following analysis: all the tautomeric forms (**I–III**) have a chelated phenolic proton that should resonate downfield close to 12–13 ppm due

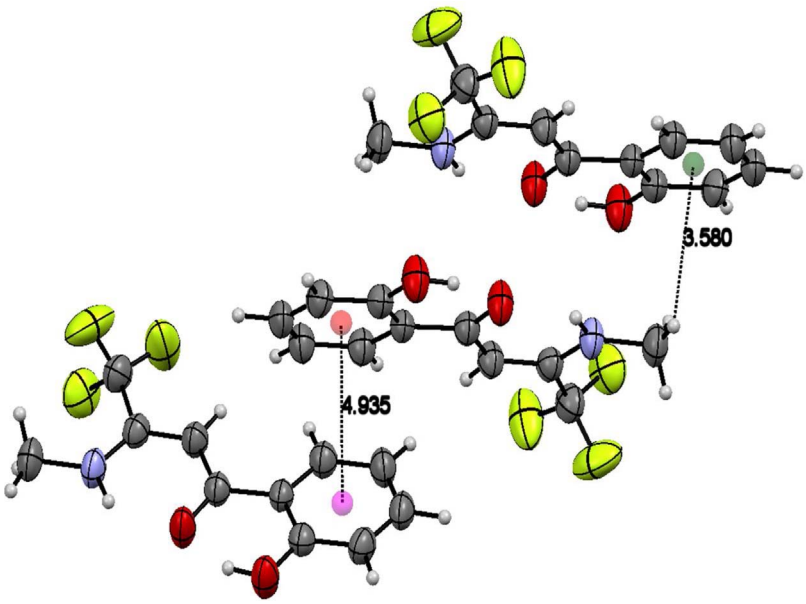

Fig. 3. Packing diagram of compound **1** showing Cg1···Cg1 and C—H···Cg1 intermolecular interactions.

to their intramolecular hydrogen bonding nature. The ^{1}H NMR shows the two most deshielded signals at 12.71 and 10.34 ppm which were assigned to the protons linked to the phenol and amino groups, respectively, hydrogen-bonded to the same carbonyl oxygen acceptor (form **I**). The lack of a signal near to 15 ppm excludes the imino-enol form since it should show a strongly deprotected signal due to a highly effective hydrogen bond between the enol donor proton and the very good acceptor sp2-hybridized nitrogen atom. In addition, the third tautomeric imino-ketone form (**III**) should also be excluded because it has only one deshielded signal. Moreover, this last form has a methylene group connecting both imino and keto groups. The corresponding signal should appear near 4–5 ppm and integrate for two hydrogen atoms. Instead, a singlet at 6.23 integrating for one hydrogen atom was found in the ^{1}H NMR spectrum. However, the multiplicity of the *N*-methyl signal is a diagnostic value, because solve the ambiguity between the imino-enol **II** and aminoenone **I** forms. The spectrum is consistent with the structure of the aminoenone (**I**) showing a broad doublet (J = 5 Hz) due to the vicinal coupling with the amino proton (N—H). The other forms should show only a singlet for this methyl group and the ^{13}C NMR spectrum confirm this structural elucidation. The most deshielded signal at 193.9 ppm is consistent with a carbonyl carbon atom, present in the aminoenone and keto-imino forms, but the signal at 88.1 ppm agrees with the methine (=CH—) carbon atom and it matches only with the aminoenone tautomer. If the equilibria were shifted to the keto-imino form, a signal close to 50 ppm would be expected, due to the methylene carbon atom.

3.3. Hirshfeld surface analysis

Hirshfeld surface analysis was performed for a better understanding of the crystal packing and the contribution of significant stabilizing intermolecular interactions of **1** and a closely related structure namely **2**. Fig. 5 shows the Hirshfeld surfaces mapped over d_{norm}, shape index and curvedness properties, in similar orientations. Contacts with distances shorter than the sum of vdW radii are visualized as red regions in the d_{norm} map, contacts close in lengths to the vdW limit are colored

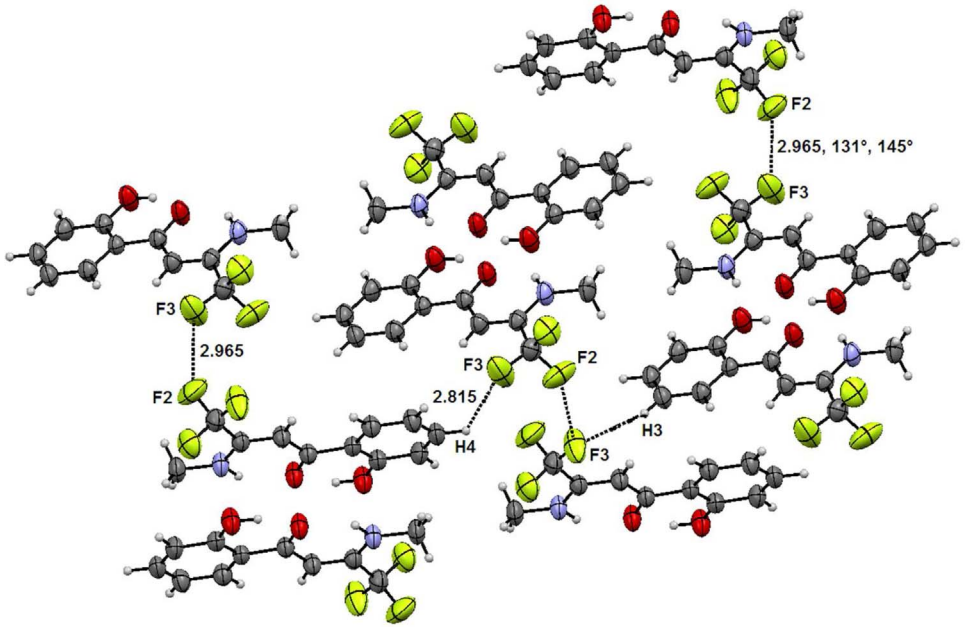

Fig. 4. Crystal packing of **1** showing C—H···F hydrogen bonds and F···F contacts.

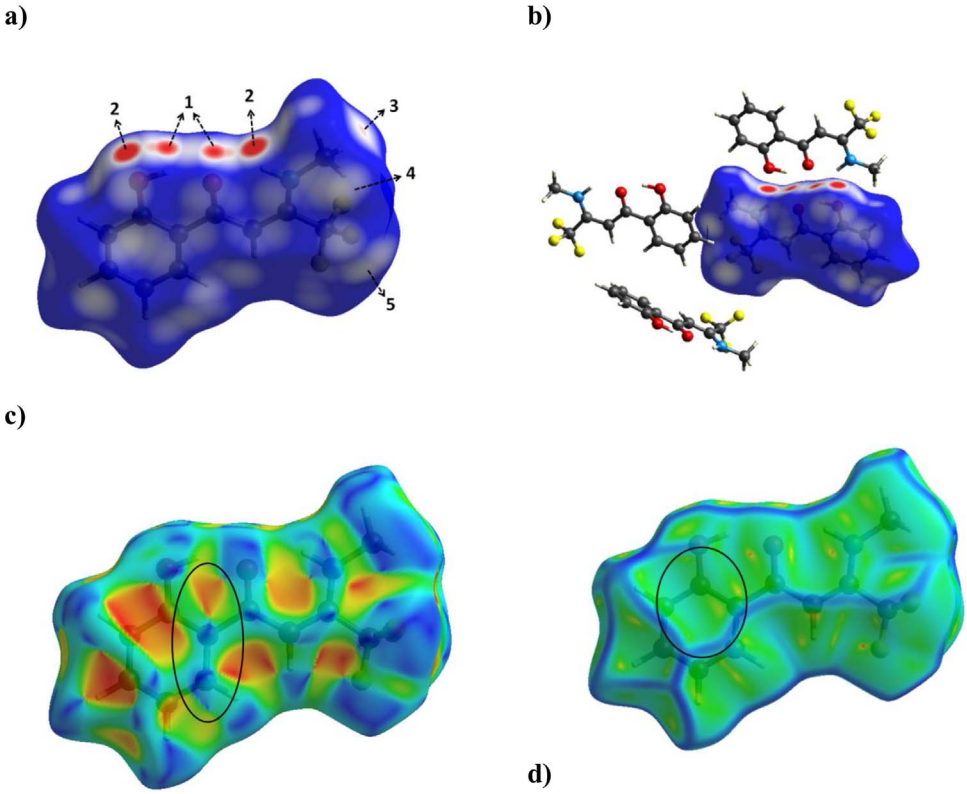

Fig. 5. Views of the Hirshfeld surfaces of **1**, mapped with (a) and (b) d_{norm}, (c) shape index and (d) curvedness properties. Close contacts are labeled as: (1) O—H···O, (2) N—H···O, (3) C—H···O, (4) C—H···F and (5) F···F.

white, while blue represents longer contacts. The large and red regions labeled as **1** in the d_{norm} map (Fig. 5a) represent O···H contacts attributed to O—H···O hydrogen bonds, which form $R_2^2(12)$ ciclic dimers (see Fig. 2). The bright red area labeled **2** are indicative of O···H interactions due to N—H···O hydrogen bonds, where the oxygen atom of the hydroxyl group acts as acceptor. These interactions are the responsible of the crystal packing of the title compound as seen in Fig. 5b. The red region located in the methyl group labeled **3** in the d_{norm} map is attributed to C—H···O hydrogen bonds involving the acceptor O1 of the hydroxyl group and one hydrogen of the methyl group of another molecule. The white spot labeled **4** on the d_{norm} surfaces are attributed to H···F contacts associated with weak C—H···F hydrogen bonds. The white region located over the fluorine atom (labeled **5**) is associated to F···F contacts, with a distance of 2.965 Å.

The Hirshfeld surface mapped with shape index (Fig. 5c) shows a pattern of alternating red and blue triangles with suitable symmetry. This is an indicative of π···π stacking interactions, as described in Section 3.1. In addition, a relatively large and flat green region at the same side of the molecule on the corresponding curvedness surface (Fig. 5d) is also characteristic of π-stacking interactions.

In this work, the Hirshfeld surface analysis was used to compare the hydrogen-bonding and π-stacking interactions of **1** with a related aminoenone, (*Z*)-4,4,4-trifluoro-3-(2-hydroxyethylamino)-1-(2-hydroxyphenyl)-2-buten-1-one (**2**) [12]. The molecular conformation of compound **2** is similar to **1**, stabilized by two strong intramolecular interactions: O—H···O and N—H···O, although their crystal packings are quite different. The supramolecular assembly of compound **2** is mainly governed by O—H···O and C—H···F hydrogen bonds and C—H···π interactions, which are visible as deep red spots labeled **1**, **4** and **6** in the d_{norm} surfaces, respectively (See Fig. S5, Supplementary information). The pattern of touching complementary pair of triangles in the shape index and the large and green flat regions for curvedness (See Fig. S5, Supplementary information) are indicative of π-stacking interactions with Cg···Cg distance of 4.2743(2) Å. This value, smaller than those measured in **1**, suggest that in **2** π-stacking interactions could play a more relevant role in the stabilization of the crystalline structure. This observation could be reinforced considering that the hydroxyphenyl interplanar distance in **1**, 3.494 Å, is also larger than those found in **2**, 3.072 and 3.478 Å.

The 2D fingerprint plots [34–36] provide evidence of intermolecular interactions including hydrogen bonds. They are used to identify different intermolecular interactions and their relative contributions can be obtained from the surface areas. The 2D fingerprint plots of **1**, displayed by the expanded view, are shown in Fig. 6. They are quite symmetric, because the interactions occur between two chemically and crystallographically identical molecules. The pair of narrow spikes at around $(d_e + d_i)$ of 2.35 Å confirm the presence of O···H/H···O hydrogen bonds with a contribution of 10.7%. The C···H/H···C contacts appear as a pair of characteristic wings around the sum $(d_e + d_i)$ of 2.95 Å, typical for C—H···π interactions (22.6%). The pair of sharp spikes in the centre of the plotcorrespond to H···F/F···H contacts, with 24.1% of contribution to the crystal packing, revealing the occurrence of intermolecular C—H···F hydrogen bonds, as described previously. The H···H interactions (as dispersive forces) are highlighted in the middle of scattered points in full 2D fingerprint map, with minima values of $(d_e + d_i)$ of around 2.4 Å. These interactions constitute the main contribution (28.4%) to the packing stabilization. The region in the centre of the fingerprint plot at around $(d_e + d_i)$ of 3.0 Å is indicative of F···F contacts, with 4.9% of the total Hirshfeld surface.

The full 2D fingerprint plot of compound **2** is shown in Fig. S6 of the Supplementary information. The H···H contacts represents the largest contribution within the Hirshfeld surface(33.1%) and is observed as one distinct pattern with a minimum value of $(d_e + d_i) \approx 2.25$ Å. The reciprocal H···F/F···H contacts appear as two symmetrical narrow pointed wings, indicating C—H···F intermolecular interactions in the crystal packing. These interactions comprise the 25.0% of the total Hirshfeld surface with $(d_e + d_i) \approx 2.45$ Å. The C···H contacts (labeled 3), with sharp pairs of spikes centered near $(d_e + d_i) \approx 2.7$ Å, with 13.1% of contribution, corresponds to C—H···C non-classical hydrogen bonds. In addition, O···H interactions (labeled 4) with symmetrical pair of spikes located at around $(d_e + d_i) \approx 2.00$ Å (12.1% of contribution) associated to O—H···O hydrogen bonds were observed. C···C contacts

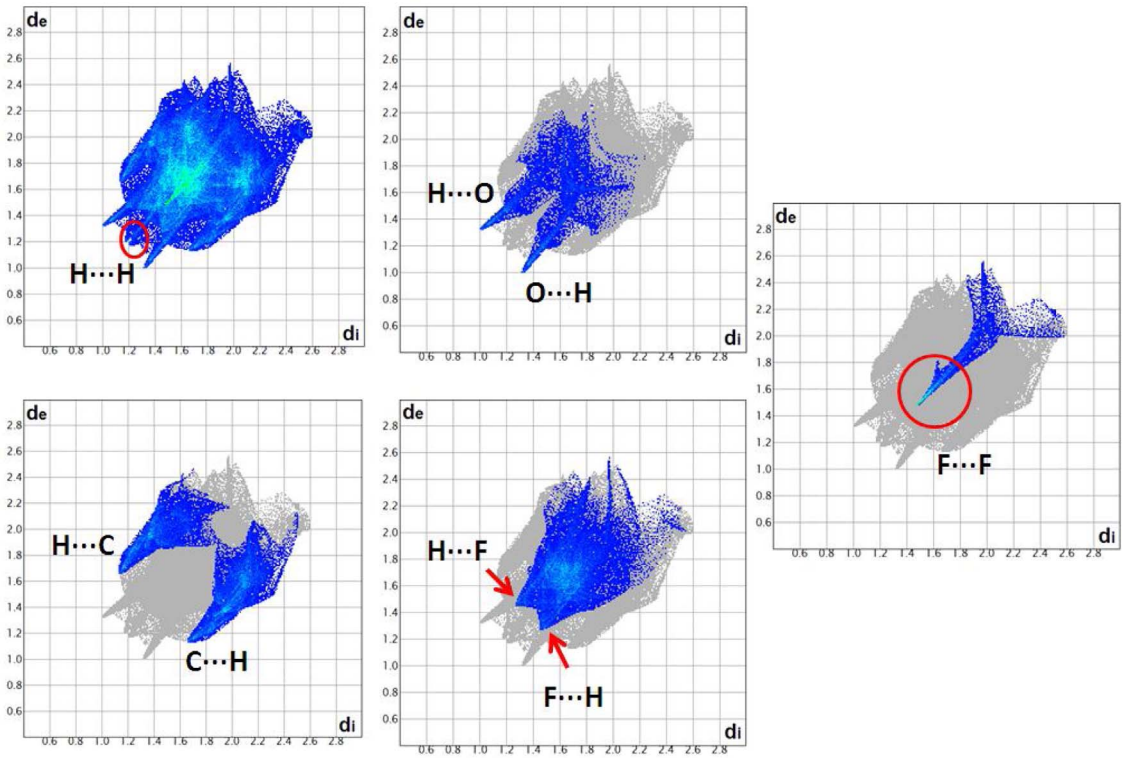

Fig. 6. Full and decomposed 2D fingerprint plots for compound **1**.

(labeled 5) attributed to characteristic π-stacking interactions between phenyl rings are clearly identified in the fingerprint plots as a green area on the diagonal at approximately 1.8 Å.

In order to analyze the propensity of two chemical species (*X* and *Y*) to be in contact, the enrichment ratios of the main intermolecular contacts of compounds **1** and **2** were calculated. The enrichment ratio (E_{XY}) of a pair of elements (*X*,*Y*) is defined as the ratio between the proportion of actual contacts in the crystal (C_{XY}) and the theoretical proportion of random contacts (R_{XY}) [49]:

$$E_{XY} = \frac{C_{XY}}{R_{XY}} \quad (1)$$

The proportion S_X of Hirshfeld surface contacts involving the pair of elements *X* and *Y* is obtained from C_{XX} and C_{XY} values. The random contacts R_{XY} could be obtained by the probability products of S_X and S_Y proportions. The enrichment ratio generally are larger than unity for pair of elements which have a high susceptibility to form contacts in the crystal, while pairs which tend to avoid contacts are associated to E_{XY} values lower than unity. The enrichment ratio of the main intermolecular contacts for compounds **1** and **2** are listed in Table S6 (Supplementary information). In **1**, the E_{CH} and E_{OH} ratios are larger than unity indicating that C···H and O···H contacts are favored in the crystal packing because of the high proportion of hydrogen atoms (S_H = 57.3%) on the Hirshfeld surface. Similar results were found for O···H interactions in **2,** but C···H contacts are disfavored. The propensity of benzene rings to form π-stacking interactions is much more extensive in compound **2** as reflected by the high value E_{CC} of 2.10, which are associated with C···C contacts. These results allow to explain the relatively low leaning observed for C···H contacts (E_{CH} = 0.81) because C···C and C···H contacts are in competition. In addition, in **1** the E_{CH} value of 1.45 indicate that C—H···π interactions could contribute to the crystal structure stabilization more than the π-stacking one, as follows from the small value of E_{CC}.

These results also suggest that the $-(CH_2)_2OH$ group in **2**, with enough flexibility to allow the formation of O—H···O hydrogen bonds (between the terminal hydroxyl and the phenol oxygen) closer to the ideal contact geometry, might promotes the formation of π-stacking interactions. Nevertheless, in **1** the favored interactions are: N—H···O, between the amine hydrogen and hydroxyl oxygen atoms; O—H···O, between the hydroxyl and carbonyl oxygen atoms (both with geometries far from the ideal) and the weak C—H···π hydrogen bond, between aromatic carbon atoms. Furthermore, for both **1** and **2**, the fluorine atom forms comparable weak intramolecular and intermolecular interactions (see Table 1). For compound **2**, the energetically favorable H···F contacts are responsible for the enrichment values higher than unity but the probability of F···F contacts is lower (E_{FF} = 0.89).

3.4. Vibrational properties

The IR and Raman spectra of the solid state compound **(1)** are shown in Fig. 7. The observed frequencies and those calculated (B3LYP/6-311 + +G(d,p)) for the isolated molecule are compared in Table S7

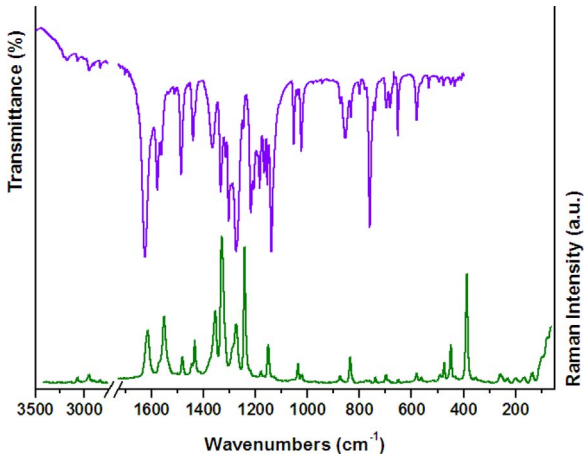

Fig. 7. IR and Raman spectra (solid) of **1**.

(Supplementary information), along with a tentative assignment. It was performed by comparison with theoretical calculations as well as with reported data for related compounds [12,50–52]. A very good agreement between the experimental and computed vibrational data was observed. The calculated frequencies were scaled due to the overestimation of force constants by the quantum chemical methods at the exact equilibrium geometry, as obtained by DFT calculations. In this work, a scale factor of 0.983 for frequencies higher than 1700 cm^{-1} and 0.958 for frequencies lower than 1700 cm^{-1} were used. The experimental and simulated IR and Raman spectra of the title compound are compiled in Figs. S7 and S8 of Supplementary information.

3.4.1. OH vibrations

The IR O—H stretching mode in phenol derivatives generally appears in the region of 3700–3500 cm^{-1}. The weak band located at 3202 cm^{-1} in the IR spectrum is assigned to the O—H stretching mode (calc. frequency: 3298 cm^{-1}). This band is very sensitive to inter- or intramolecular hydrogen bonds. The presence of ortho substituents (such as O, S, N, F, Cl, Br and I) or unsaturated moieties (such as C═O, C═C, C═N) produces a red shift of the OH band due to intramolecular hydrogen bonding effect. The crystal structure of **1** revealed that the intramolecular hydrogen bonding is formed via a six-membered ring structure O—H···O(keto) and N—H···O(keto) (see Fig. 1), usually known as chelation. This kind of hydrogen bonding results in a lower O—H stretching frequency (3200–2500 cm^{-1}), and the IR bands are generally extremely broad.

The absorptions attributed to the O—H in-plane and out-of-plane bending modes in phenols are found in the regions of 1400–1300 cm^{-1} and 710–517 cm^{-1}, respectively. The IR band located at 1365 cm^{-1} (1355 cm^{-1} in Raman) is assigned to O—H in-plane bending mode. In accordance with the potential energy distribution, it is strongly coupled with the C—C stretching modes of the phenyl ring. The OH out-of-plane bending mode is observed at 800 cm^{-1} in the IR and Raman spectra, with 82% of PED contribution.

3.4.2. C═O vibrations

The close examination of the C═O stretching mode region reveals a strong absorption at 1561 cm^{-1} in the IR spectrum, with a counterpart in Raman at 1551 cm^{-1}. The experimental values are well-reproduced by the quantum chemical calculations, with computed ν(C═O) value of 1593 cm^{-1}. The low calculated value found for the C═O force constant is associated with two intramolecular O—H···O═C and N—H···O═C hydrogen bonds involving the C═O group.

The C═O in-plane bending mode was assigned to the band at 778 cm^{-1}, which is strongly coupled with the out-of-plane C—H bending modes. The IR band at 683 cm^{-1} (687 cm^{-1} in Raman) is attributed to the C═O out-of-plane bending mode.

3.4.3. N—H vibrations

The N—H stretching vibrations are generally observed as weak and sharp bands in the 3500–3300 cm^{-1} spectral region [53]. When the N—H is involved in intra or intermolecular hydrogen bonding interactions, this band shifts to lower frequencies. The N—H stretching mode was not observed in the IR spectrum of the title compound due to its low intensity and by overlapping with the broad band of the O—H group attached to the ring. The medium absorption at 1334 cm^{-1} is tentatively assigned to the N—H in-plane bending mode.

3.4.4. CH_3 vibrations

The observed weak band located at 3066 cm^{-1} is assigned to the CH_3 asymmetric stretching mode (Raman, 3066 cm^{-1}). These results are in agreement with the computed frequency at 3107 cm^{-1}. The weak absorption at 2948 cm^{-1} is tentative assigned to CH_3 symmetric stretching vibration. The CH_3 asymmetric bending modes appear as a weak band at 1434 cm^{-1} in the IR spectrum (1433 cm^{-1} in Raman). These assignments are in accordance with reported data in literature [53] and with the calculated values (see Table S7, Supplementary information). The very weak IR absorption at 1384 cm^{-1} (with weak Raman counterpart at 1373 cm^{-1}) is assigned to the CH_3 symmetric bending mode.

3.4.5. Phenyl ring vibrations

The C—H stretching modes of substituted benzenes usually give rise to the IR and Raman bands in the 3200–3000 cm^{-1} region. The IR absorptions observed as weak bands at 3174 and 3141 cm^{-1}, with a counterpart at 3140 cm^{-1} in Raman, are attributed to the C—H stretching modes of the phenyl ring. The in-plane C—H bending modes appear as a series of bands at 1440 and 1154 cm^{-1} in the IR spectrum (Raman at 1145 and 1151 cm^{-1}, respectively). These results are in agreement with the computed frequencies (see Table S7). The weak IR bands located at 944, 875, 833 and 761 cm^{-1} (874, 836 and 764 cm^{-1} in Raman) are assigned to the C—H out-of-plane bending mode of the phenyl ring.

The C—C stretching modes usually appear as prominent bands in the infrared and Raman spectra of aromatic derivatives, and they are generally influenced by substituents [53]. The infrared spectrum of the title compound (see Fig. 6 and Table S7) shows strong bands at 1618, 1577 and 1023 cm^{-1} (1614, 1569 and 1022 cm^{-1} in Raman) that are tentatively assigned to the C—C stretching modes of the phenyl ring. These results are in agreement with the computed values reported in the Supplementary information (Table S7).

3.4.6. CF_3 vibrations

The assignment of all CF_3 vibrational modes is given in Table S7. The IR spectrum shows two intense absorptions at 1166 and 1138 cm^{-1}, with Raman counterparts at 1167 and 1130 cm^{-1}, which are attributed to the CF_3 asymmetric stretching modes. The lower intensity band at 1040 cm^{-1} in the Raman spectrum is assigned to the CF_3 symmetric stretching vibration. The CF_3 IR bending modes are located at 698 cm^{-1} (symmetric) and at 579 and 494 cm^{-1} (asymmetric). These frequency values and the relative intensities are in very good agreement with the computed ones, as shown in Table S7.

3.5. NBO and AIM topological analysis

The Natural Bond Orbital (NBO) analysis is an important tool for the rationalization of hydrogen bonds that correlates well with the changes in bond distances in agreement with the basic chemical concepts. It is also used to obtain information on changes in charge densities at proton donor and acceptor sites as well as in the bonding and antibonding orbitals. For each donor (i) and acceptor (j), the stabilization energy $E^{(2)}$ associated with the delocalization (i) → (j) is estimated with the following formula [31]:

$$E^{(2)} = q_i \frac{F(i,j)^2}{\varepsilon_i - \varepsilon_j} \quad (2)$$

where q_i is the orbital occupancy, ε_i and ε_j are the diagonal elements and *F(i,j)* is the off-diagonal NBO Fock matrix element. In NBO analysis of hydrogen bonds systems, the charge transfer between the lone pairs of proton acceptor and antibonding orbital of proton donor is the most significant. The interaction energy $E^{(2)}$ between the lone pair of atom Y and σ* of the X—H bond correlates to the intensity of the X—H···Y interaction. This value provides a measure of how much the stabilization achieved through the complexes formed by hydrogen bond interaction contributes to the total interaction energy. NBO calculations have been performed at B3LYP/6-311 + + G(d,p) level to investigate the relative strength of all hydrogen bonds (intra and intermolecular). The stabilization energies between lone pair electrons of proton acceptor and antibonding orbitals of the proton donor are listed in Table 2. As discussed above, the planar molecular conformation of compound **1** is stabilized by two intramolecular hydrogen bonding interactions

Table 2
Second-order perturbation theory analysis of the Fock matrix for compound **(1)** calculated at B3LYP/6-311 + + G(d,p) approximation.

Interaction (donor → acceptor)[a]	$E^{(2)}$ (Kcal mol^{-1})[b]
lp N → π* C8—C9	61.44
lp_{π} O2 → σ* C1—C7	12.10
lp_{π} O2 → σ* C7—C8	14.59
π C8-C9 → π* C7—O2	28.03
π C2-C3 → π* C4—C5	21.73
π C4-C5 → π* C2—C3	16.04
Intramolecular	
lp O2 → σ* N—H	4.17
lp O2 → σ* O—H	5.42
Intermolecular	
lp O1 → σ* N—H	6.98
lp O2 → σ* O1—H	4.20

[a] For atoms numbering see Fig. 1; lp denotes the lone pair on the specified atom.
[b] $E^{(2)}$ indicates energy of the hyperconjugative interactions.

involving the O2 of the carbonyl group as the sole acceptor. Comparing the both intramolecular interactions between the lone pairs of O2 and the O1—H and N—H antibonding orbitals, NBO analysis showed that the former (lp O2 → σ* O1—H) is more stabilizing than the latter, (lp O2 → σ* N—H) in approximately 1.3 kcal mol^{-1}. It is in accordance with the correlation observed between hydrogen bond length and stabilization energy $E^{(2)}$. The intramolecular hydrogen bond O—H···O(keto) has the shorter bond length ($R_{O2\cdots H}$ = 1.725 Å) and the larger stabilization energy, indicating that this interaction is the strongest hydrogen bond.

In the structure of the title compound, the lp O1 participates as electrons donor and the σ* (N—H) antibonding orbital as electrons acceptor in intermolecular hydrogen bonding interactions and contributes to the complex stabilization in about 6.98 kcal mol^{-1}. The O—H···O (keto) hydrogen bonds are involved in lp O2 → σ* (O1—H) intermolecular interactions, and the intermolecular charge transfer which causes stabilization of the hydrogen bond is estimated in approximately 4.20 kcal mol^{-1}. The NBO analysis confirmed that the hydrogen bonded structure of the title compound is principally stabilized by intermolecular N—H···O1 and O—H···O(keto) interactions, having the former the shorter bond length ($R_{H\cdots O1}$ = 2.356 Å) and the higher stabilization energy, resulting stronger compared to O—H···O(keto) hydrogen bond.

The NBO analysis is also important to study other interesting electronic properties of the central O═C—C═C—N moiety. The lone pair of the N atom (low electron occupancy of 1.792e) contributes to a strong mesomeric interaction with the C8═C9 double bond. The calculated stabilization energy for the interaction lp N → π* C8—C9 is 61.44 kcal mol^{-1}. The electron donation into the π* C8—C9 antibonding orbital is reflected in the high population for this vacant molecular orbital, with an electron occupancy of 0.322e. This strong donor-acceptor interaction can be associated with resonance structure in which the bond N—C9 has a partial double bond character. A high lp N → π* C8—C9 interaction value is associated with a shortening of the N—C bond distance.

The atoms in molecules theory (AIM) is a very useful tool to analyze and characterize the strength of the hydrogen bonding interactions. The formation of hydrogen bonds is associated with the presence of a bond critical point (BCP) between the hydrogen atom of a donor group and an acceptor atom, which are linked by the associated bond path. The molecular graph of the centrosymmetric dimer performed using AIM2000 program is shown in Fig. S9 of Supplementary information. The topological parameters such as electron density (ρ), Laplacian of electron density ($\nabla^2(\rho)$), electron kinetic energy density (K), potential electron energy density (V), total electron energy density (H) and hydrogen bond energy ($E_{H\cdots X}$) at the BCPs in the considered molecular association have been evaluated by means of the AIM method at B3LYP/6-311 + + G(d,p) theory level (Table 3).

For the analyzed system, the intramolecular hydrogen bonds form six-membered rings and hence the ring critical points (RCP) also exist. It is well known that greater electron density at RCP corresponds to stronger intramolecular hydrogen bond (see Fig. S9, Supplementary information). The results indicate that the O—H···O(keto) intramolecular hydrogen bond has the maximum value of electron density at the RCP (0.01827 a.u.) compared with N—H···O(keto) contacts (0.01568 a.u.) indicating clearly that the former is the strongest hydrogen bond. As was discussed previously, the strength and length of the chemical bond are closely correlated. The strength of the hydrogen bond is determined by accumulation of electron density in the bond region and the screening of nuclei by this density. According to the previously discussed, the O—H···O(keto) intermolecular hydrogen bond has the largest electron density value at the H···O BCP (0.0449 a.u.), see Table 3.

AIM calculations showed that values of $\rho(r)$ are in the range 0.0081–0.0449 a.u. and 0.00598–0.0098 a.u. for intramolecular and intermolecular hydrogen bonds, respectively. The low values of charge density and positive values of its Laplacian, $\nabla^2(\rho)$, at the BCPs indicate the presence of significant hydrogen bonding interactions, in accordance with the criteria proposed by Koch and Popelier [54].

One of the most important features of the hydrogen bonds is its energy. In this work, the AIM method was used to estimate the hydrogen bond energy $E_{H\cdots X}$. Espinosa and co-workers proposed a relation between hydrogen bond energy $E_{H\cdots X}$ and potential electron energy density (V) at the BCP [34]. As observed in Table 3, the strongest intramolecular hydrogen bond ($E_{H\cdots X}$ = 12.05 kcal mol^{-1}) is the O—H···O(keto) interaction. These results agree with those previously mentioned.

Two topological parameters both the total electron energy density (H) and Laplacian $\nabla^2(\rho)$ at BCP are useful to characterize the strength of hydrogen bonds. In accordance to Rozas et al. [55], the strength of the interactions may be classified as follow: weak H-bonds are characterized by $\nabla^2(\rho)$ and H > 0 and $E_{H\cdots X}$ < 12.0 kcal mol^{-1}; medium H-

Table 3
Topological parameters obtained from AIM analysis considering molecular associations.

Interaction	*d(H···X)*	ρ_{BCP}	$\nabla^2(\rho)$	*G*	*V*	*H*	*E (H···X)*
Intramolecular							
O—H···O(keto)	1.724	0.0449	0.149	0.0378	0.0384	0.0762	12.1
N—H···O(keto)	1.877	0.0334	0.109	0.0276	0.0279	0.0555	8.74
C—H11A···F1	2.534	0.0081	0.042	0.0084	0.0062	0.0146	1.95
C—H11C···F2	2.496	0.0098	0.051	0.0103	0.0079	0.0182	2.48
Intermolecular							
N—H···O(H)	2.356	0.0098	0.038	0.0086	0.0077	0.0163	2.42
O—H···O(keto)	2.449	0.0081	0.0379	0.0081	0.0067	0.0148	2.11
C—H11B···O(H)	2.724	0.0059	0.0250	0.00503	0.00381	0.0088	1.19

ρ: electron density (a.u.); $\nabla^2(\rho)$): Laplacian of electron density at the BCP (a.u.); G: Lagrangian kinetic energy (a.u.); V: Potential electron energy density at BCP (a.u.); H: Halmitonian kinetic energy (a.u.); E(H···X): hydrogen bond energy (kcal mol^{-1}). Distances H···X (X = O, F) in Å.

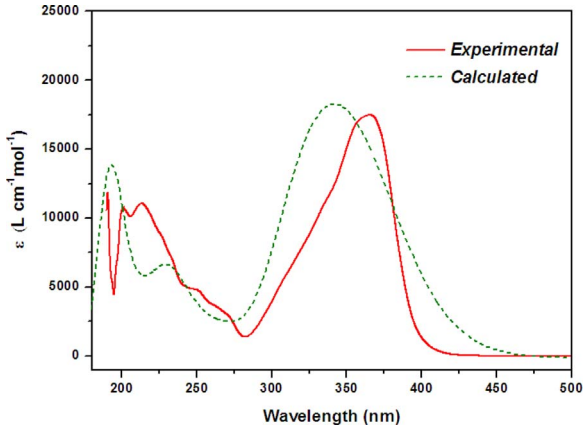

Fig. 8. Experimental and calculated electronic spectra of compound **(1)**.

bonds are characterized by $\nabla^2(\rho) > 0$, $H < 0$ and $E_{H\cdots X}$ in the range 12.0–24.0 kcal mol^{-1} and strong H-bonds are characterized by $\nabla^2(\rho)$ and $H < 0$ and $E_{H\cdots X} > 24.0$ kcal mol^{-1}. Based on the topological parameters listed in Table 3, all analyzed hydrogen bonds (intra and intermolecular) are weak and mainly of electrostatic character [55].

3.6. Electronic properties and UV–vis spectra

Fig. 8 shows the experimental and calculated UV–vis spectra of **1**. The transitions with contributions greater than 10% are shown in Table 4, and only the dominant excitations (chosen in accordance with their oscillator strength) are used to assign the observed bands. In accordance with these results, a very good agreement between the experimental and computed electronic spectra was observed.

The experimental spectrum shows an intense band at 365 nm (computed value: 359 nm), assigned to a one electron transition from HOMO to LUMO molecular orbitals. The HOMO → LUMO transition has a π → π* character. The absorption located at 337 nm is mainly associated with HOMO-1 → LUMO (92%) transition, in accordance with the calculated value of 322 nm. The observed band at 264 nm attributed to singlet electron promotion from HOMO-2 to LUMO (80%), is originated principally by excitations from non bonding orbitals to π* of the aromatic ring (calc. 266 nm). The weak band at 251 nm is mainly due to dominant excitation from HOMO-1 → LUMO + 1 transitions (96%). The bands located at 227, 214 and 201 nm in the experimental electronic spectrum are essentially attributed to HOMO → LUMO + 2 (90%), HOMO-2 → LUMO + 1 (61%) and HOMO-4 → LUMO (50%), respectively. These results are in agreement with the computed values (See Table 4).

Fig. 9 shows the frontier molecular orbitals involved in the main electronic transitions, together with their energies (in eV). These orbitals were considered to assign the experimental bands in the electronic spectra.

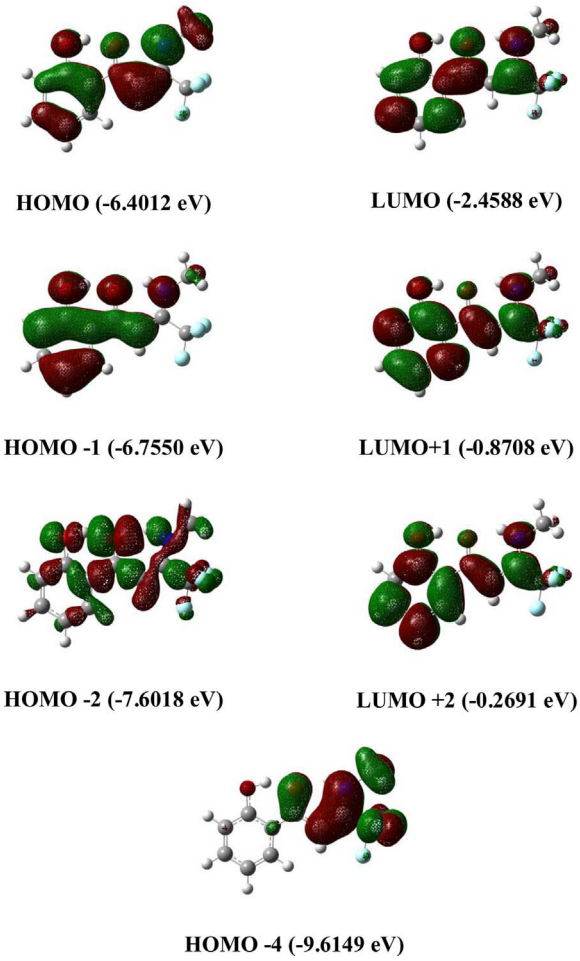

Fig. 9. Frontier molecular orbitals of **1** involved in the main electronic transitions. Calculated energies are also given.

The HOMO corresponds to a π-bonding character localized over the phenyl ring with contributions of p-type lone pair orbital of the oxygen and the N atom atoms. The HOMO-1 displays π −bonding character involving the phenyl ring and in the aminoenone moiety with non-bonding contribution of the oxygen and N atoms. Moreover, the HOMO-4 corresponds to a π- bonding system localized over the O═C−C═C−N moiety with the contribution of the p-type lone pair

Table 4
Experimental and calculated absorption wavelengths (nm), energy transitions (eV), oscillator strengths and tentative assignment for most relevant electronic transitions of **1**.

Wavelength (nm)		Energy (eV)	Oscillator strength (*f*)	Assignment
Experimental[a]	Calculated[b]			
365	359	3.4535	0.3711	HOMO → LUMO (92%)
337	322	3.8506	0.3165	HOMO-1 → LUMO (92%)
264	266	4.6644	0.0602	HOMO-2 → LUMO (80%) HOMO → LUMO + 1 (20%)
251	234	5.2963	0.1478	HOMO-1 → LUMO + 1 (96%)
227	218	5.6784	0.0682	HOMO → LUMO + 2 (90%)
214	193	6.4219	0.2605	HOMO-2 → LUMO + 1 (61%) HOMO-4 → LUMO (20%)
201	191	6.4752	0.1361	HOMO-4 → LUMO (50%) HOMO-2 → LUMO + 2 (27%)

[a] UV–vis spectrum in ethanol solution (5.64×10^{-5} M).
[b] TD-B3LYP/6-311 + + G(d,p) level in ethanol.

orbitals of the fluorine atoms.

The LUMO frontier molecular orbital exhibits some π* contributions of the carbon atoms on the benzene ring and the aminoenone moiety. The LUMO + 1 and LUMO + 2 exhibit predominantly extended π antibonding character on phenyl ring and aminoenone moiety, in addition to non-bonding contribution of the oxygen oxygen and N atom atoms.

4. Conclusions

The single crystal XRD method showed that the studied compound corresponds to the aminoenone tautomer, the *(Z)*-4,4,4-trifluoro-1-(2-hydroxyphenyl)-3-(methylamino)-2-buten-1-one **(1)**. The molecule in the crystal lattice adopts a planar conformation and the *Z*-configuration favors the N—H and O—H hydrogen bonds to the central acceptor carbonyl oxygen atom. Intramolecular hydrogen bond interaction between the O2 of the carbonyl group and the hydroxyl and the N—H group forming a six-member ring favors the planar conformation observed for the compound. The particularly strong intramolecular interactions N—H and O—H bonded to the same acceptor C═O oxygen atom are predominant and restrict similar N—H and O—H interactions between neighboring molecules, leading to intermolecular interactions without the ideal geometry. This behaviour points out the relevance of the mentioned intramolecular interactions, which determine not only the molecular conformation but also influence in the supramolecular architecture by weakening the conventional hydrogen intermolecular bonds. The packing of molecules in the crystal is held by O—H···O(keto) and N—H···O hydrogen bonds. Furthermore, C—H···π, F···F and π-stacking interactions were also found to contribute to crystal stabilization.

The Hirshfeld surfaces and their associated 2D Fingerprint plots proved to be useful in the study of the intermolecular interactions and their quantitative contributions to the crystal packing of compound **1**. It suggests that in **1**, C—H···π hydrogen bonds could play a significantly role in the stabilization of the crystal structure while in **2**, likely due to the $-(CH_2)_2OH$ group, π-stacking interactions could be favored. In addition, the enrichment ratios calculated from the Hirshfeld surface analysis allowed us to quantify the likelihood of the main intermolecular interactions to form the supramolecular assembly of the title compound, as well as in a related compound. The inter- and intramolecular detected using NBO and AIM analysis, agree with the experimental data. After spectroscopic elucidation by ^{1}H, ^{13}C and ^{19}F NMR, it can be deduced that the structure of the molecule dissolved in $CDCl_3$ reveals the same tautomeric and E/Z configurational preference as in the crystal lattice. The described results allow us to conclude that the title compound exist as a unique species, the Z-isomer of the β-aminoenone tautomer.

Acknowledgements

The authors thank Universidad Nacional de La Plata (UNLP), CONICET, DAAD-Germany, and Departamento de Ciencias Básicas de la Universidad Nacional de Luján for financial support. S.E.U and J.L.J specially thanks Deutscher Akademischer Austauschdienst Germany (DAAD) for an equipment grant and CONICET (PIP 0359) for financial support. D.M.G. and M.R. thank ANPCyT (PICT-2016-0226) for financial support. The crystallographic work was supported by CONICET (PIP 1529), and by ANPCyT (PME06 2804 and PICT06 2315) of Argentina. S.E.U, G.A.E, O.E.P and D.M.G are research fellows of CONICET. J.L.J is research fellow of Comisión de Investigaciones Cientificas (CIC). M.R. thanks CONICET for doctoral fellowship.

Appendix A. Supplementary data

Supplementary data associated with this article can be found, in the online version, at https://doi.org/10.1016/j.jfluchem.2018.01.001.

References

[1] S. Kovács, Z. Novák, Copper on iron promoted one-pot synthesis of β-aminoenones and 3,5-disubstituted pyrazoles, Tetrahedron 69 (2013) 8987–8993.
[2] I.O. Edafiogho, S.B. Kombian, K.V. Ananthalakshmi, N.N. Salama, N.D. Eddington, T.L. Wilson, M.S. Alexander, P.L. Jackson, C.D. Hanson, Enaminones: exploring additional therapeutic activities, J. Pharm. Sci. 96 (2007) 2509–2531.
[3] N.D. Eddington, Enaminones-versatile therapeutic pharmacophores. Further advances, Curr. Med. Chem. 7 (2000) 417–436.
[4] N.N. Salama, N.D. Eddington, D. Payne, T.L. Wilsonb, Multidrug resistance and anticonvulsants: new studies with some enaminones, Curr. Med. Chem. 11 (2004) 2093–2113.
[5] I.O. Edafiogho, et al., Synthesis, characterization and anticonvulsant activity of enaminones, J. Med. Chem. 35 (1992) 2798–2805.
[6] S.B. Kombian, I.O. Edafiogho, K.V. Ananthalakshmi, Anticonvulsant enaminones depress excitatory synaptic transmission in the rat brain by enhancing extracellular GABA levels, Br. J. Pharmacol. 145 (2005) 945–953.
[7] K.R. Scott, et al., Synthesis and anticonvulsant activity of enaminones. 2. Further structure-activity correlations, J. Med. Chem. 36 (1993) 1947–1955.
[8] K.R. Scott, et al., Synthesis and anticonvulsant activity of enaminones. 3. Investigations on 4′-, 3′-, and 2′-substituted and polysubstituted anilino compounds, sodium channel binding studies, and toxicity evaluations, J. Med. Chem. 38 (1995) 4033–4043.
[9] S. Doherty, R. John Errington, N. Housley, J. Ridland, W. Clegg, M.R.J. Elsegood, *N*-Alkoxy-β-ketoiminate complexes of groups 4 and 5: synthesis and characterization of the complexes $[(\eta^5\text{-}C_5H_4R)M\{CH_3C(O)CHC(NCH_2CHR'O)CH_3\}Cl_n]$ (M = Ti, n = 1; M = Nb, n = 2; R = H, me; R' = H, me), $[Ti\{CH_3C(O)CHC(NCH_2CHR'O)CH_3\}Cl_2(thf)]$, and $[Ti\{CH_3C(O)CHC(NCH_2CHR'O)CH_3\}_2]$, Organometallics 18 (1999) 1018–1029.
[10] J. Kim, J.W. Hwang, Y. Kim, M.H. Lee, Y. Han, Y. Do, Synthesis, structure and ethylene polymerization behavior of zirconium complexes with chelating ketoiminate ligands, J. Organomet. Chem. 620 (2001) 1–7.
[11] D.L. Chizhov, M.G. Pervova, M.A. Samorukova, E.F. Khmara, V.I. Filyakova, V.I. Saloutin, V.N. Charushin, Trialkyl borate assisted amination of fluorinated 1,3-diketones for synthesis of N,N′-1,2-phenylen-bis(β-aminoenones) and their Ni(II), Cu(II) and Pd(II) complexes, J. Fluor. Chem. 132 (2011) 394–401.
[12] A. Hidalgo, L.P. Avendaño Jiménez, L.A. Ramos, M.A. Mroginski, J.L. Jios, S.E. Ulic, G.A. Echeverría, O.E. Piro, E. Castellano, Spectroscopic, structural, and conformational properties of (Z)-4,4,4-trifluoro-3-(2-hydroxyethylamino)-1-(2-hydroxyphenyl)-2-buten-1-one, $C_{12}H_{12}F_3NO_3$: a trifluoromethyl-substituted β-aminoenone, J. Phys. Chem. A 116 (2012) 1110–1118.
[13] Y.M. Chumakov, V.I. Tsapkov, G. Bocelli, B. Ya Antosyak, N-Acetyl-4-[(2-hydroxybenzylidene)amino]benzenesulfonamide monohydrate and N-acetyl-4-[(5-bromo-2-hydroxybenzylidene)amino]benzenesulfonamide monohydrate, Acta Cryst. C61 (2005) o460–o463.
[14] M. Yildiz, H. Ünver, D. Erdener, N.O. Iskeleli, Spectroscopic studies and crystal structure of 4-(2-hydroxy-3-methoxybenzylideneamino)-N-(5-methylisoxazol-3-yl) benzenesulfonamide, J. Chem. Crystallogr. 40 (2010) 691–695.
[15] A. Subashini, M. Hemamalini, P. Thomas Muthiah, G. Bocelli, A. Cantoni, Synthesis and crystal structure of a new schiff base 4-[(2-hydroxy-benzylidene)-amino]-N-(5-methyl-isoxazol-3-yl)-benzenesulfonamide, J. Chem. Crystallogr. 39 (2009) 112–116.
[16] G.O. Dudek, R.H. Holm, Nuclear magnetic resonance studies of keto-enol equilibria. III. α,β-Unsaturated-β-ketoamines, J. Am. Chem. Soc. 84 (1962) 2691–2696.
[17] Y.C. Shi, $R_2^2(14)$ dimers in 3-(hydroxyethyl)amino-1-phenylbut-2-en-1-one, Acta Cryst. E61 (2005) o2005–o2007.
[18] Y.C. Shi, C.X. Sui, H.M. Yang, 1-Phenyl-3-[(1-phenylethyl)amino]but-2-en-1-one, Acta Cryst. E61 (2005) o3574–o3575.
[19] K.J. Akerman, O.Q. Munro, An X-ray crystallographic and density functional theory study of (3Z)-4-(5-ethylsulfonyl-2-hydroxyanilino)pent-3-en-2-one and (3Z)-4-(5-tert-butyl-2-hydroxyanilino)pent-3-en-2-one, Acta Cryst. C69 (2013) 258–262.
[20] A. Jezierska, L.B. Jerzykiewicz, J. Kolodziejczak, J.M. Sobczak, Synthesis, X-ray crystal structure and DFT study of potential ligands of (2Z)-3-[(2-hydroxyphenyl) amino]-1-phenylalk-2-en-1-one type, J. Mol. Struct. 839 (2007) 33–40.
[21] B.E. Smart, Fluorine substituent effects (on bioactivity), J. Fluor. Chem. 109 (2001) 3–11.
[22] CrysAlisPro, Oxford Diffraction Ltd., version 1.171.33.48 (release 15-09-2009 CrysAlis171. NET).
[23] G.M. Sheldrick, A short history of SHELX, Acta Crystallogr. A 4 (2008) 112–122.
[24] M.J. Frisch, J.A. Pople, J.S. Binkley, J. Chem. Phys. 80 (1984) 3265;
M.J. Frisch, G.W. Trucks, H.B. Schlegel, G.E. Scuseria, M.A. Robb, J.R. Cheeseman, J.A. Montgomery Jr., T. Vreven, K.N. Kudin, J.C. Burant, J.M. Millam, S.S. Iyengar, J. Tomasi, V. Barone, B. Mennucci, M. Cossi, G. Scalmani, N. Rega, G.A. Petersson, M. Nakatsuji, M. Hada, K. Ehara, R. Toyota, J. Fukuda, M. Hasegawa, T. Ishida, Y. Honda, O. Kitao, H. Nakai, M. Klene, X. Li, J.E. Knox, H.P. Hratchian, J.B. Cross, C. Adamo, J. Jaramillo, R. Gomperts, R.E. Stratmann, O. Yazyev, A.J. Austin, R. Cammi, C. Pomelli, J.W. Ochterski, P.Y. Ayala, K. Morokuma, G.A. Voth, P. Salvador, J.J. Dannenberg, V.G. Zakrzewski, S. Dapprich, A.D. Daniels, M.C. Strain, O. Farkas, D.K. Malick, A.D. Rabuck, K. Raghavachari, J.B. Foresman, J.V. Ortiz, Q. Cui, A.G. Baboul, S. Clifford, J. Cioslowski, B.B. Stefanov, G. Liu, A. Liashenko, P. Piskorz, I. Komaromi, R.L. Martin, D.J. Fox, T. Keith, M.A. Al-Laham, C.Y. Peng, A. Nanayakkara, M. Challacombe, P.M.W. Gill, B. Johnson, W. Chen, M.W. Wong, C. González, J.A. Pople, Gaussian 03, Revision C.02, Gaussian Inc., Wallingford, CT, 2004.
[25] A.D. Becke, Density-functional thermochemistry. III. The role of exact exchange, J.

Chem. Phys. 98 (1993) 5648.
[26] C. Lee, W. Yang, R.G. Parr, Development of the Colle-Salvetti correlation-energy formula into a functional of the electron density, Phys. Rev. B 37 (1988) 785.
[27] M.H. Jamróz, Vibrational energy distribution analysis (VEDA): scopes and limitations, Spectrochim. Acta A 114 (2013) 220.
[28] M.H. Jamróz, Vibrational Energy Distribution Analysis VEDA4, (2004) Warsaw.
[29] R.E. Stratmann, G.E. Scuseria, M.J. Frisch, An efficient implementation of time-dependent density-functional theory for the calculation of excitation energies of large molecules, J. Chem. Phys. 109 (1998) 8218–8224.
[30] M. Cossi, N. Rega, G. Scalmani, V. Barone, Energies, structures, and electronic properties of molecules in solution with the C-PCM solvation model, J. Comput. Chem. 24 (2003) 669.
[31] A.E. Reed, L.A. Curtis, F. Weinhold, Intermolecular interactions from a natural bond orbital, donor-acceptor viewpoint, Chem. Rev. 88 (1988) 899.
[32] R.F.W. Bader, Atoms in Molecules: A Quantum Theory, Oxford University Press, Oxford, 1990.
[33] E. Espinosa, E. Molins, C. Lecomte, Hydrogen bond strengths revealed by topological analyses of experimentally observed electron densities, Chem. Phys. Lett. 285 (1998) 170–173.
[34] J.J. McKinnon, D. Jayatilaka, M.A. Spackman, Towards quantitative analysis of intermolecular interactions with Hirshfeld surfaces, Chem. Commun. (2007) 3814–3816.
[35] M.A. Spackman, D. Jayatilaka, Hirshfeld surface analysis, CrystEngComm 11 (2009) 19–32.
[36] J.J. McKinnon, M.A. Spackman, A.S. Mitchell, Novel tools for visualizing and exploring intermolecular interactions in molecular crystals, Acta Crystallogr. 60B (2004) 627–668.
[37] S.K. Wolf, D.J. Grimwood, J.J. McKinnon, M.J. Turner, D. Jayatilaka, M.A. Spackman, Crystal Explorer (Version 3.1), University of Western Australia, 2012.
[38] P. Gilli, V. Bertolasi, V. Ferretti, G. Gilli, Evidence for intramolecular N–H...O resonance-assisted hydrogen bonding in β-enaminones and related heterodienes. A combined crystal-structural, IR and NMR spectroscopic, and quantum-mechanical investigation, J. Am. Chem. Soc. 122 (2000) 10405–10417.
[39] P. Subramaniam, C. Ramasubbu, S. Athiramu, Exploiting intramolecular hydrogen bonding for the highly (Z)-selective & metal free synthesis of amide substituted β-aminoenones, Green Chem. 19 (2017) 2541–2545.
[40] P. Panini, D. Chopra, Role of intermolecular interactions involving organic fluorine in trifluoromethylated benzanilides, CrystEngComm 14 (2012) 1972–1989.
[41] R. Berger, G. Resnati, P. Metrangolo, E. Weber, J. Hulliger, Organic fluorine compounds: a great opportunity for enhanced materials properties, Chem. Soc. Rev. 40 (2011) 3496.
[42] D. Chopra, T.N. Guru Row, Role of organic fluorine in crystal engineering, CrystEngComm 13 (2011) 2175.
[43] D. Chopra, Is organic fluorine really not polarizable? Cryst. Growth Des. 12 (2012) 541–546.
[44] A.R. Choudhury, T.N. Guru Row, Organic fluorine as crystal engineering tool: evidence from packing features in fluorine substituted isoquinolines, CrystEngComm 8 (2006) 265.
[45] D. Chopra, V. Thiruvenkatam, S.G. Manjunath, T.N. Guru Row, Variability in halogen interactions: in situ cryocrystallization of low melting substituted trifluoroacetophenones, Cryst. Growth Des. 7 (2007) 868–874.
[46] V. Vasylyeva, O.V. Shishkin, A.V. Maleev, K. Merz, Crystal structures of fluorinated pyridines from geometrical and energetic perspectives, Cryst. Growth Des. 12 (2012) 1032–1039.
[47] A.R. Choudhury, R.G. Bhat, T.N. Guru Row, S. Chandrasekaran, Weak Csp3–H...F–C interaction overshadows the strong C⋮C–H...OC hydrogen bond: structure of pentafluorophenyl prop-2-ynyl carbonate, Cryst. Growth Des. 7 (2007) 844.
[48] R.J. Baker, P.E. Colavita, D.M. Murphy, J.A. Platts, J.D. Wallis, Fluorine–fluorine interactions in the solid state: an experimental and theoretical study, J. Phys. Chem. A 116 (2012) 1435–1444.
[49] C. Jelsch, K. Ejsmont, L. Huder, The enrichment ratio of atomic contacts in crystals, as indicator derived from the Hirshfeld surface analysis, IUCrJ 1 (2014) 119–128.
[50] L.P. Avendaño Jiménez, G.A. Echeverría, O.E. Piro, S.E. Ulic, J.L. Jios, Vibrational, electronic, and structural properties of 6-nitro- and 6-amino-2-trifluoromethylchromone: an experimental and theoretical study, J. Phys. Chem. A 117 (2013) 2169–2180.
[51] C.D. Alcívar León, G.A. Echeverría, O.E. Piro, S.E. Ulic, J.L. Jios, A detailed experimental and theoretical study of two novel substituted trifluoromethylchromones. The influence of the bulky bromine atom on the crystal packing, Spectrochim. Acta A 136 (2015) 1358–1370.
[52] C.D. Alcívar León, G.A. Echeverría, O.E. Piro, S.E. Ulic, J.L. Jios, M. Burgos Paci, G.A. Argüello, The role of halogen $CX_1\cdots X_2C$ contact on the preferred conformation of 2-perhalomethylchromones in solid state, Chem. Phys. 472 (2016) 142–155.
[53] D. Lin-Vien, N.B. Colthup, W.G. Fateley, J.G. Grasselli, The Handbook of Infrared and Raman Characteristic Frequencies of Organic Molecules, Academic Press Inc., United Kingdom, 1991.
[54] U. Koch, P. Popelier, Characterization of CHO hydrogen bonds on the basis of the charge density, J. Phys. Chem. A 99 (1995) 9747.
[55] I. Rozas, I. Alkorta, J. Elguero, Behavior of ylides containing N O, and C atoms as hydrogen bond acceptors, J. Am. Chem. Soc. 122 (2000) 11154.